Promoting Effects of La for Improved Oxygen Reduction Activity and High Stability of Pt on PtLa Alloy Electrodes

Sung Jong Yoo,[a] Seung Jun Hwang,[a] June-Gunn Lee,[b] Seung-Cheol Lee,[b] Tae-Hoon Lim,[a] Yung-Eun Sung,[c] Andrzej Wieckowski,[d] and Soo-Kil Kim*[e]

[a]Fuel Cell Research Center, Korea Institute of Science and Technology, 39-1 Hawolgok-dong, Seoul 136-791, Korea.

[b]Computational Science Center, Korea Institute of Science and Technology, 39-1 Hawolgok-dong, Seoul 136-791, Korea.

[c]World Class University Program of Chemical Convergence for Energy & Environment, School of Chemical and Biological Engineering, Seoul National University, Shinlimdong 56-1, Seoul 151-742, Korea.

[d]Department of Chemistry, University of Illinois at Urbana-Champaign, Urbana, IL 61801, USA.

[e]School of Integrative Engineering, Chung-Ang University, 221, Heukseok-Dong, Dongjak-Gu, Seoul, 156-756, Korea. E-mail: sookilkim@cau.ac.kr; Fax: +82-2-814-2651; Tel: +82-2-820-5770

*Address correspondence to this author. Tel: 82-2-820-5770, Fax: 82-2-958-5199, E-mail: sookilkim@cau.ac.kr

1. Bulk composition analysis

The electron microprobe, known as the electron probe micro-analyzer, uses X-ray spectrometry to identify and measure concentration of elements in microscopic volumes of the specimen. Before examining the catalytic activity and stability, the electrodes were characterized by thermal field emission electron probe micro-analyzer (FE-EPMA) (JXA-8500F) combining high SEM resolution with high quality X-ray analysis of sub-micronareas. This FE-EPMA were maintained under high vacuum, in the pressure range of $2x10^{-5}$ - 10^{-6} torr (about one-billionth of the atmospheric pressure), by a combination of mechanical and diffusion pumps. This FE-EPMA had the capability of lowering the radius of interaction volume down to as small as 0.5 μm so that accurate composition measurements for thin intermetallic layers can be performed. In this study, at least four measurements were made for every phase and the average value was reported. A focused electron beam at an accelerating voltage of 6 kV and an emission current of 10 nA were used to detect characteristic x rays from the label elements (Pt and La atoms).

Figure S1 shows the FE-EPMA spectra for the Pt-La electrodes, respectively. Evidently all the peaks correspond to those characteristic of Pt and La. According to these spectra, in the near surface region the compositions of the Pt-La electrodes were (a) ~96 % Pt and ~4 % La, (b) ~85 % Pt and ~15 % La, (c) ~74 % Pt and ~26 % La, (d) ~67 % Pt and ~33 % La, (e) ~60 % Pt and ~40 % La, and (f) ~52 % Pt and ~48 % La.
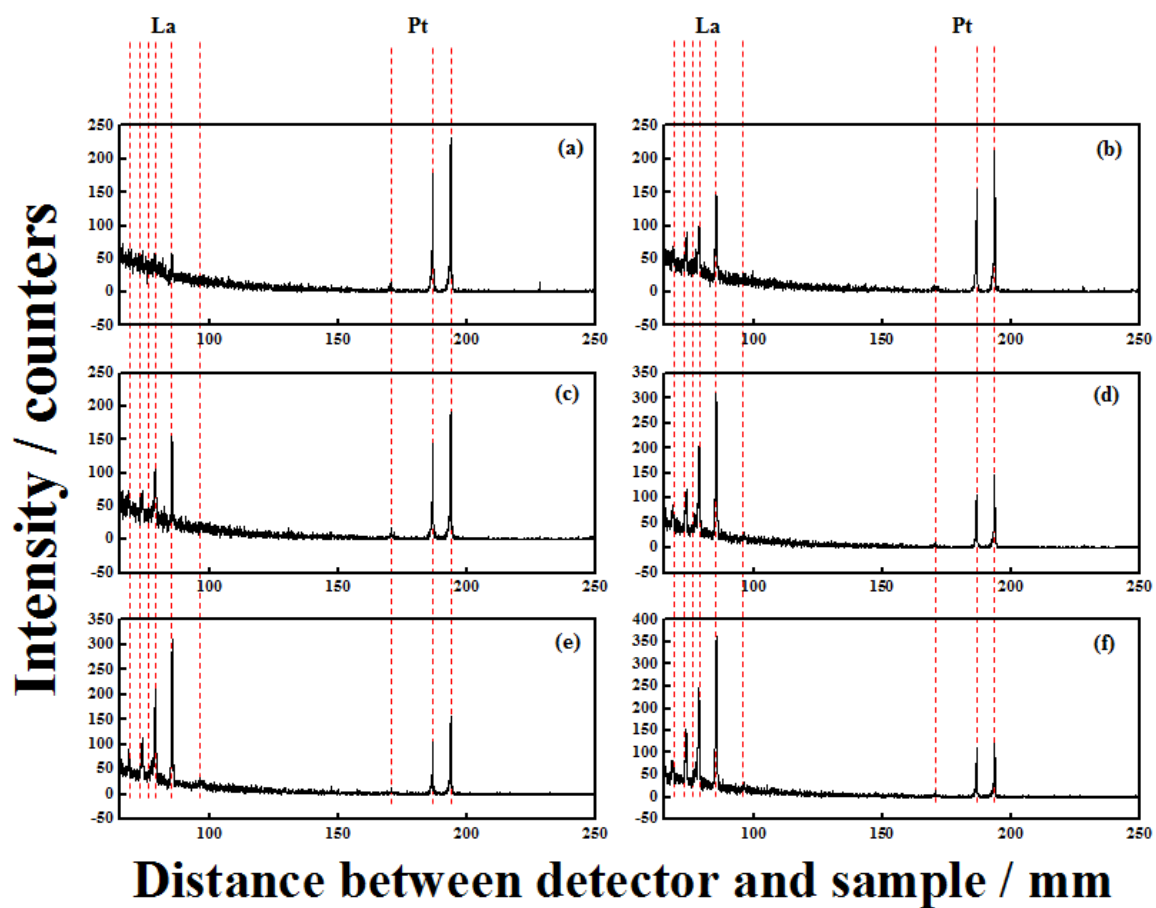
Figure S1. *FE-EPMA spectra of Pt-La electrodes. (a) ~96 % Pt and ~4 % La, (b) ~85 % Pt and ~15 % La, (c) ~74 % Pt and ~26 % La, (d) ~67 % Pt and ~33 % La, (e) ~60 % Pt and ~40 % La, and (f) ~52 % Pt and ~48 % La.*

2. **Sample perpetration and electrochemical characterization using a rotating disk electrode**

Pt–La alloy electrodes were grown using a radio-frequency (RF) magnetron co-sputtering system comprising a dual sputtering gun. Si (100) and glassy carbon were used as substrates to characterize the structural and electrochemical properties, respectively. Co-sputtering was performed under inert Ar gas at a flow rate of 26 sccm at room temperature for 10 min, and this produced films with a thickness of approximately 213 nm. In order to fabricate Pt–La thin-film electrodes with various compositions, the guns with the metal targets in the RF magnetron sputtering system were controlled as a function of the RF power. As the RF power of the La target gun was increased at a fixed RF power of the Pt gun, the La concentration was varied from 0 % to 48 %.

An AutoLab PGSTAT20 potentiostat and a rotating disk electrode (RDE) system (Ecochemie) with a conventional three-electrode configuration were used for all the electrochemical measurements. All the electrochemical measurements, except for the ORR with the RDE configuration, were performed in an Ar-purged 0.1 M $HClO_4$ solution. For the ORR experiment, 99.99 % oxygen gas was bubbled into the electrolyte for 60 min before each measurement. A catalyst-coated glassy carbon electrode with a diameter of 5 mm was used as the working electrode. Before each measurement, the glassy carbon electrode was polished with a 0.05-μm alumina paste followed by washing with distilled (DI) water in an ultrasonic bath. A saturated calomel electrode (SCE) with 3 M KCl (Gamry) and a glassy carbon rod were used as the reference and counter electrodes, respectively. However, in this paper, all the potentials reported are with respect to the Reversible Hydrogen Electrode (RHE).

The ORR measurements were performed in 0.1 M $HClO_4$ solutions under flow of O_2 (research grade) using the glassy carbon rotating disk electrode (RDE) at a rotation rate of 1600 rpm and a sweep rate of 10 mV s^{-1}. In order to produce a clean electrode surface, several potential sweeps between 0.05 and 1.1 V versus RHE were applied to the electrode prior to the ORR measurement. In the ORR polarization curve, current densities were normalized in reference to the geometric area of the glassy

carbon RDE (0.196 cm^2).

For the ORR at a RDE, the Koutecky-Levich equation can be described as follows:

$$1 / i = 1 / i_k + 1 / i_{l,c} = 1 / i_k + 1 / (0.62 n F A D_0^{2/3} \omega^{1/2} v^{-1/6} C_0^*) \text{--} (1)$$

where i is the experimentally measured current, $i_{l,c}$ is the diffusion-limiting current, and i_k is the kinetic current; where D_0 is the diffusivity of oxygen in 0.1 M HClO$_4$ (estimated from the product of O$_2$ diffusivity at infinite dilution and the ratio of the dynamic viscosities of the electrolyte and pure water), n is the number of electrons in the O$_2$ reduction reaction (i.e., $n = 4$), v is the kinematic viscosity of the electrolyte, c_0 is the solubility of O$_2$ in 0.1 M HClO$_4$, and ω is the rotation rate. Then, the kinetic current was calculated based on the following equation:

$$i_k = (i \times i_{l,c}) / (i_{l,c} - i) \text{--} (2)$$

For each catalyst, the kinetic current was normalized to the real surface area (0.202 cm^2). The accelerated durability tests were performed at room temperature in O$_2$ saturated 0.1 M HClO$_4$ solutions by applying cyclic potential sweeps between 0.6 and 1.1 V versus RHE at a sweep rate of 50 mV s^{-1} for a given number of cycles.
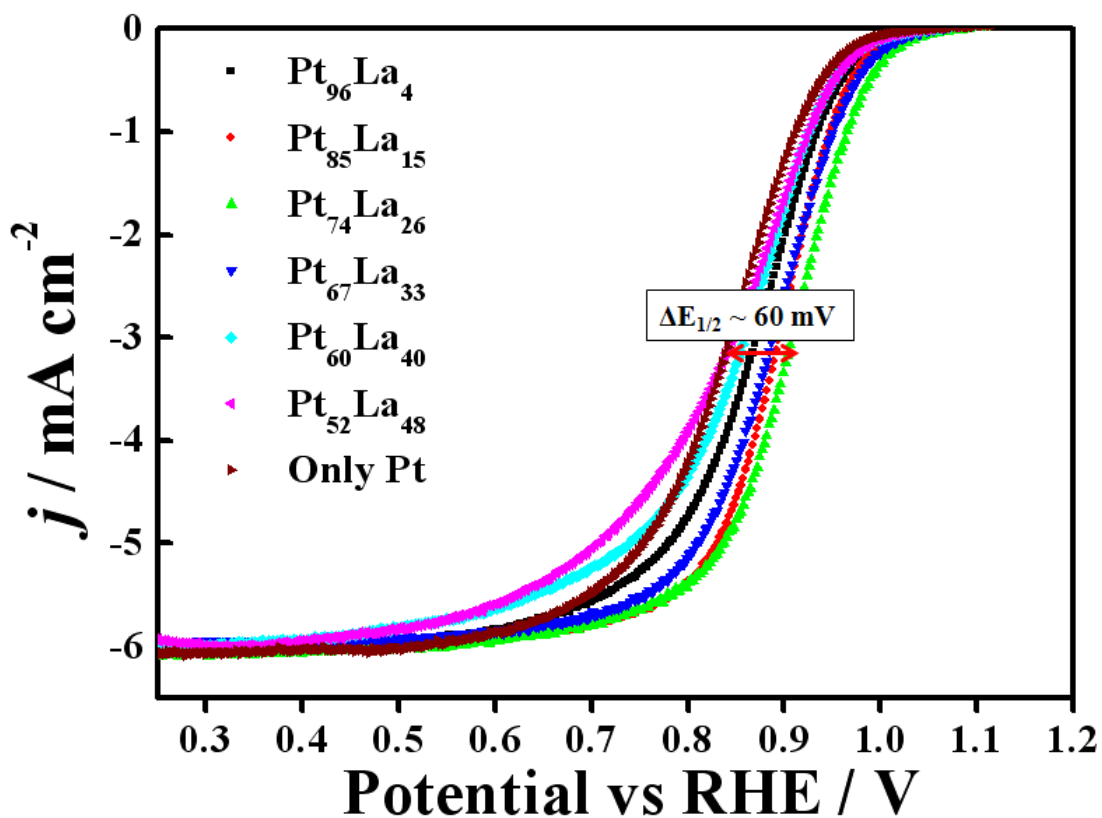
Figure S2. *Oxygen reduction reaction (ORR) polarization curves using Pt–La alloy electrodes with various compositions in a 0.1 M HClO$_4$ solution; sweep rate was 10 mV s^{-1} and rotating rate was 1600 rpm.*
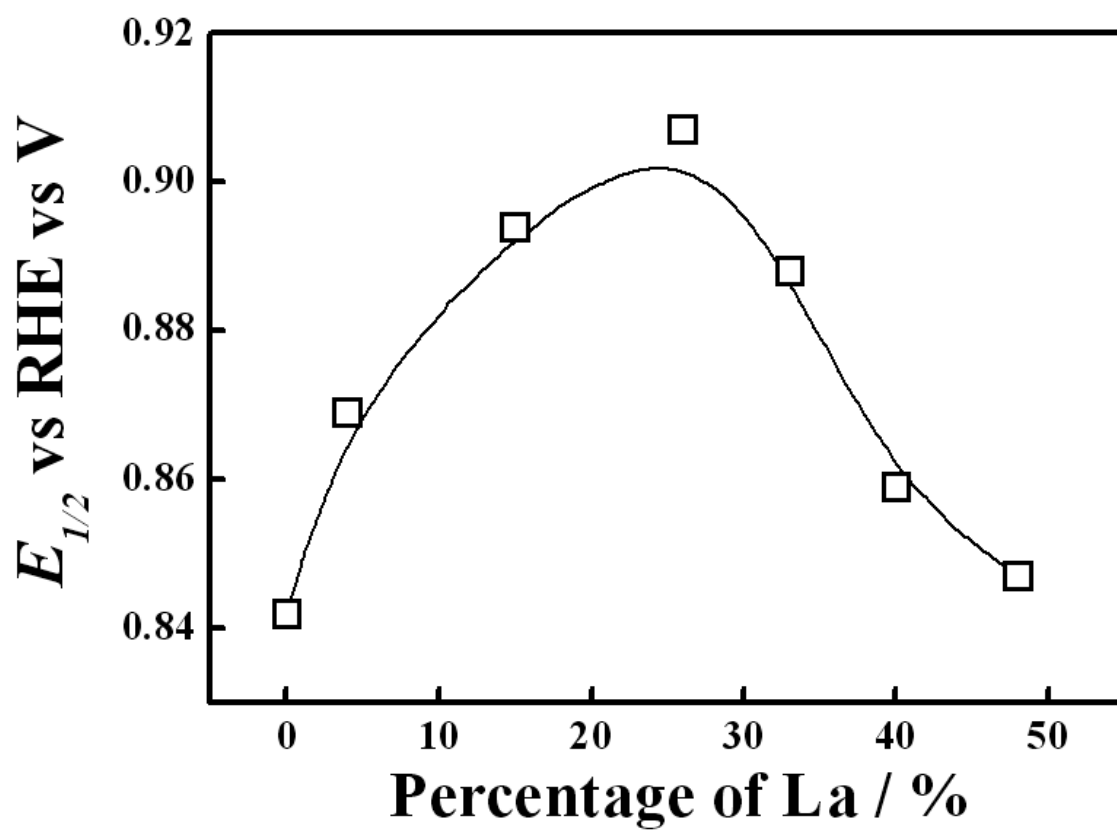
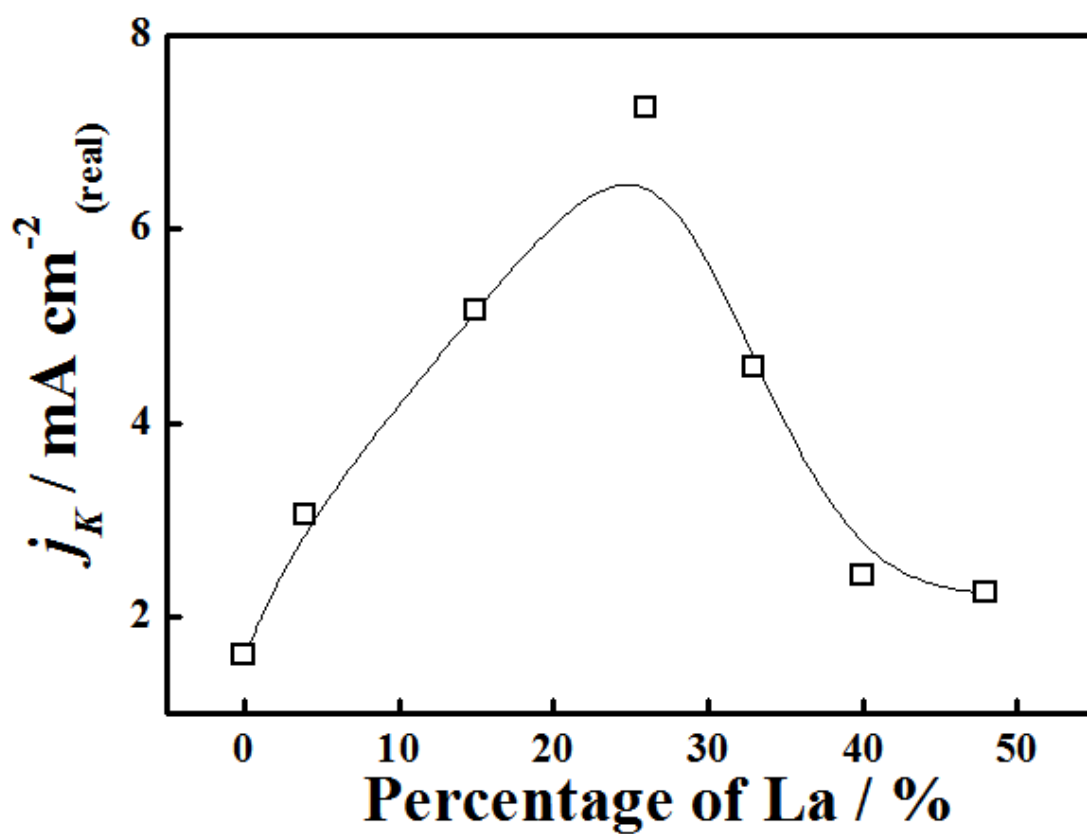***Figure S3.*** *Relationship between the half-wave potential and the degree of alloying of Pt-La.*

Figure S4. Relationship between the kinetic current density (at 0.9 V) and the degree of alloying of Pt-La.
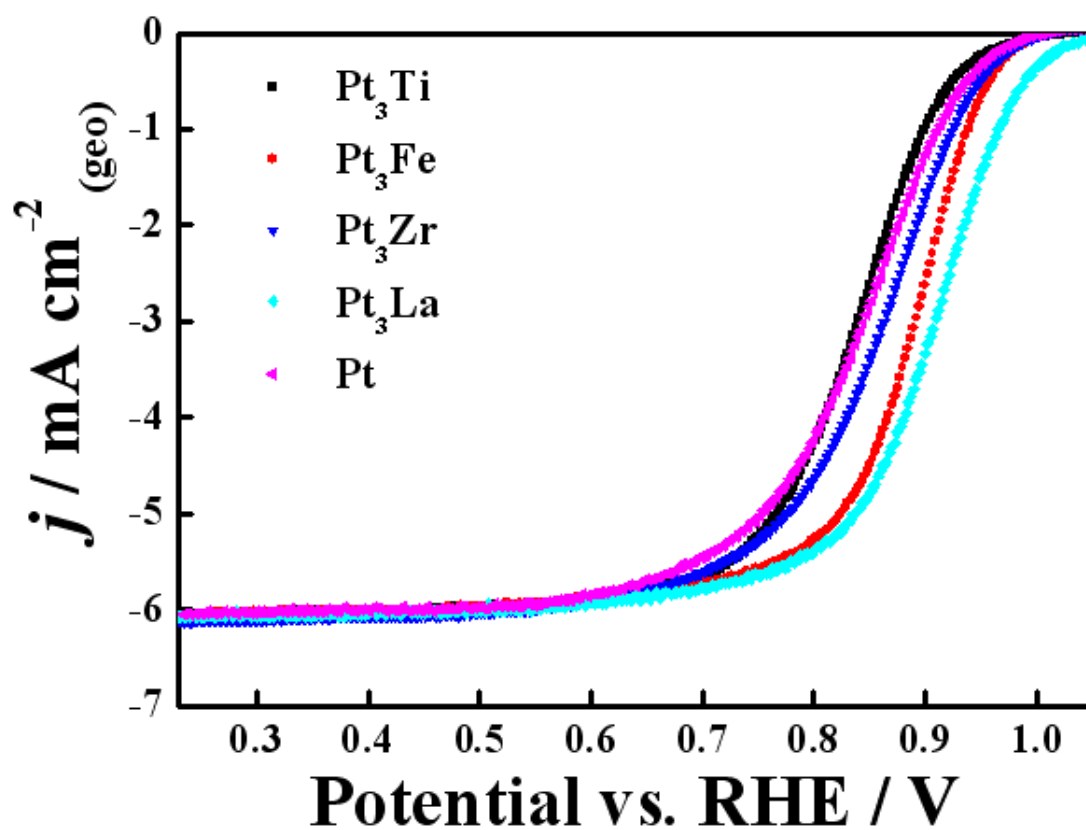
Figure S5. *Polarization curves obtained using a rotating disk electrode for O$_2$ reduction on Pt$_3$M (M=Ti, Fe, Zr, and La) alloy and pure Pt electrodes in 0.1 M HClO$_4$. Rotating rate, 1600 rpm; sweep rate, 10 mV s^{-1}.*
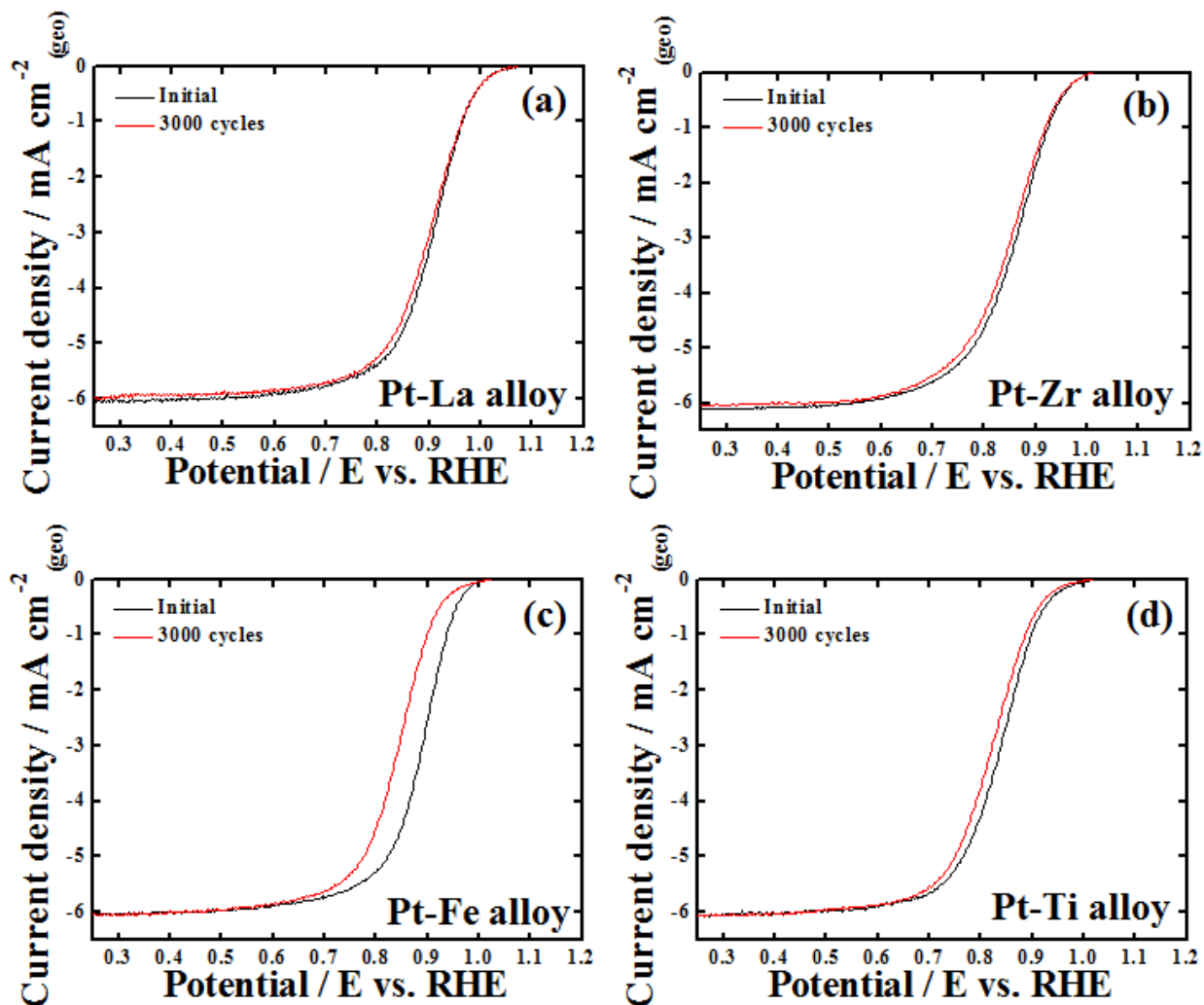
Figure S6. *A comparison of the first steady cycle (black line) and after 3000 cycles (red line), for (a) Pt₃La, (b) Pt₃Zr alloy, (c) Pt₃Fe alloy, and (d) Pt₃Ti alloy. Measurements were taken at 10 mV s⁻¹ and 1600 rpm.*

3. Confirmation of the electrochemically active surface area

The CO-stripping measurement was used to estimate the real surface area of the electrodes, following the procedures. The 0.1 M $HClO_4$ solution was purged with Ar gas for 30 min prior to electrochemical measurements. For CO-stripping measurements, pure CO was bubbled into the electrolyte under potential control at 0.1 V vs. NHE for 30 min. Then, the electrolyte was purged for 30 min with Ar gas, while keeping the electrode potential at 0.1 V vs. NHE to eliminate the dissolved CO in the electrolyte. The first anodic scan (scan speed: 10 mV s^{-1}) was performed to electro-oxidize the adsorbed CO and the subsequent voltammetry in order to verify the completeness of the CO oxidation. Assuming that each Pt surface atom is covered by a single adsorbed CO molecule, the charge for electro-desorption of CO should be 420 μC cm^{-2}. Figure S7 shows the voltammograms of Pt and Pt_3La in the presence and the absence of CO. The integrated CO stripping charge for all voltammograms came to 85.0 ± 0.5 μC, irrespective of the electrode composition. This suggests that the geometric (0.196 cm^2) and real surface areas are almost equal (about 0.202 ± 0.01 cm^2)..
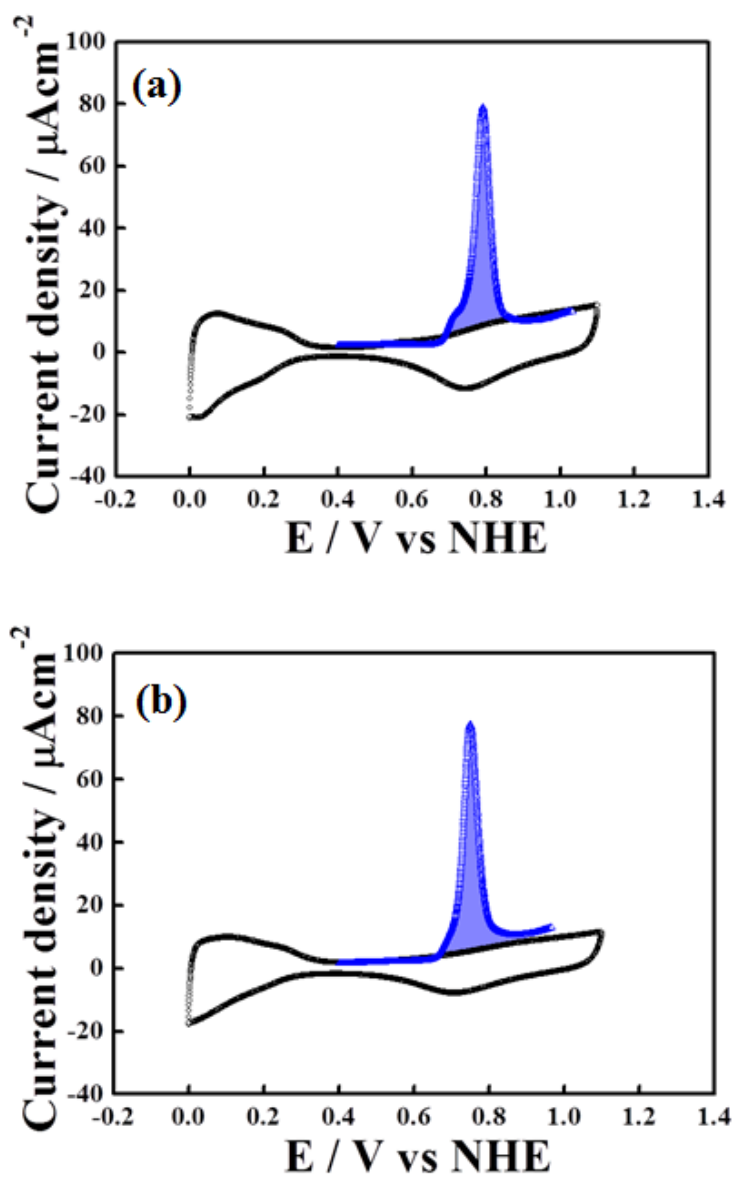
Figure S7. *CO stripping voltammetry of (a) Pt and (b) Pt₃La after CO adsorption at 0 V vs NHE for different adsorption times. During CO stripping Ar in working electrode compartment (flow rate 120 ml min^{-1}). Sweep rate 10 mV s^{-1}. Room temperature.*

4. Synchrotron X-ray diffraction

X-ray diffraction (XRD) data were measured at 8C2 high-resolution powder diffraction beamline of Pohang Accelerator Laboratory (PAL). For the XRD, The incident X-rays were vertically collimated by a mirror, and monochromatized to the wavelength of 1.5490 Å using a double-crystal Si(111) monochromator. The detector arm of the vertical scan diffractometer is composed of seven sets of soller slits, flat Ge(111) crystal analyzers, anti-scatter baffles, and scintillation detectors, with each set separated by 20°. Each specimen was prepared by flat plate side loading method to avoid preferred orientation, and the sample was then rotated about the normal to the surface during the measurement in order to increase sampling statistics. Step scan was performed at room temperature from 30° in 2θ with 0.02° increment and 1° overlaps to the next detector bank up to 80° in 2θ.
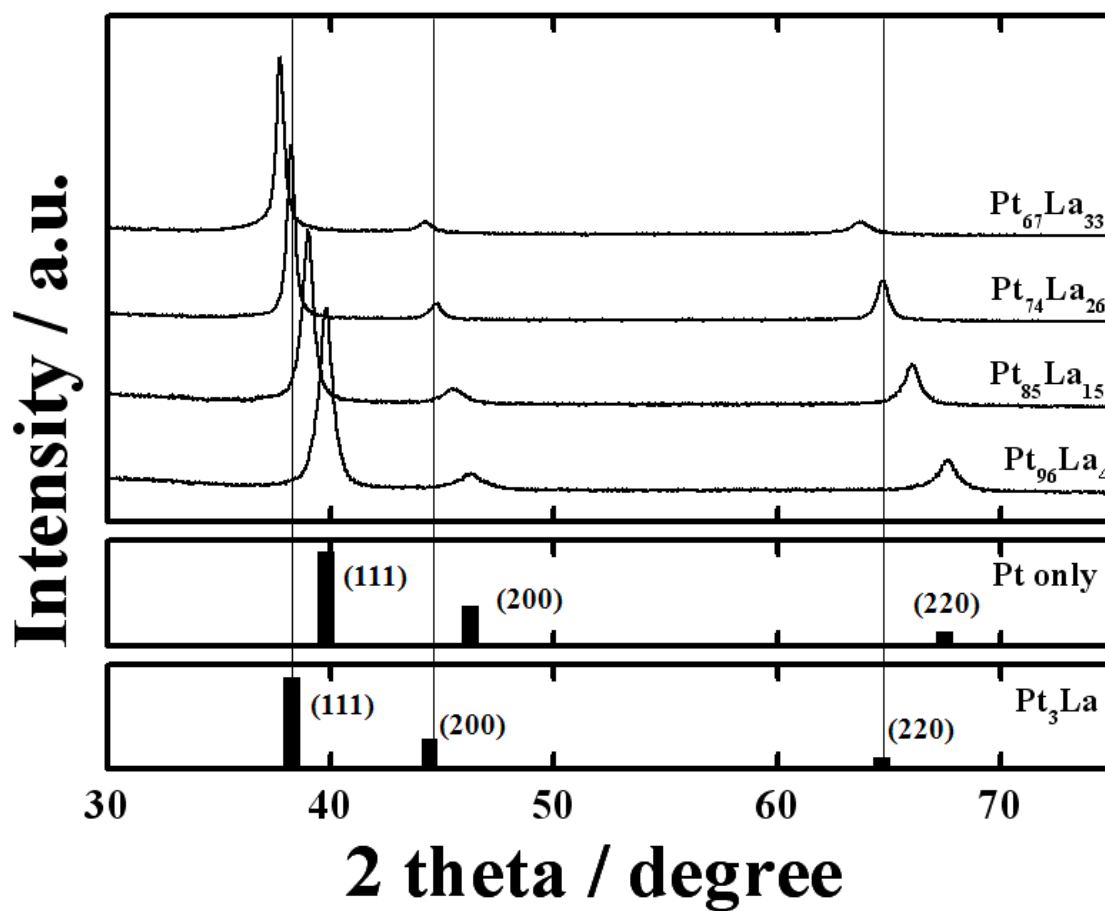
Figure S8. *X-ray diffraction patterns of the Pt and Pt-La alloy catalysts studied in this work.*

5. Synchrotron high-resolution X-ray photoelectron spectroscopy

High-resolution X-ray photoelectron spectroscopy (HR-XPS) measurements were performed on the soft X-ray beamline (8A1) connected to an undulator (U7) at the Pohang Accelerator Laboratory (PAL). The end station was composed of a high performance electron analyzer (SCIENTA-200) with energy and angular resolution of 5 meV and 0.5°, respectively. The experiment was carried out in an ultrahigh vacuum (UHV) chamber with a base pressure $\leq 5 \times 10^{-10}$ Torr. All spectra were measured using 630 eV of incident photon energy. The Shirley background is subtracted from the measured spectra. The position of the center of the valence band is given by $\int N(\varepsilon)\varepsilon \, d\varepsilon / \int N(\varepsilon) \, d\varepsilon$, where $N(\varepsilon)$ is the DOS or, in our case, the XPS-intensity after background subtraction [1],[2]. The background-subtracted spectra were integrated up to 10.0 eV BE with respect to E_F, which is calculated from the Au film as a reference. Figure S9 shows the HR-XPS valence band (d-band) spectra from the Pt$_3$M and only Pt electrode samples.
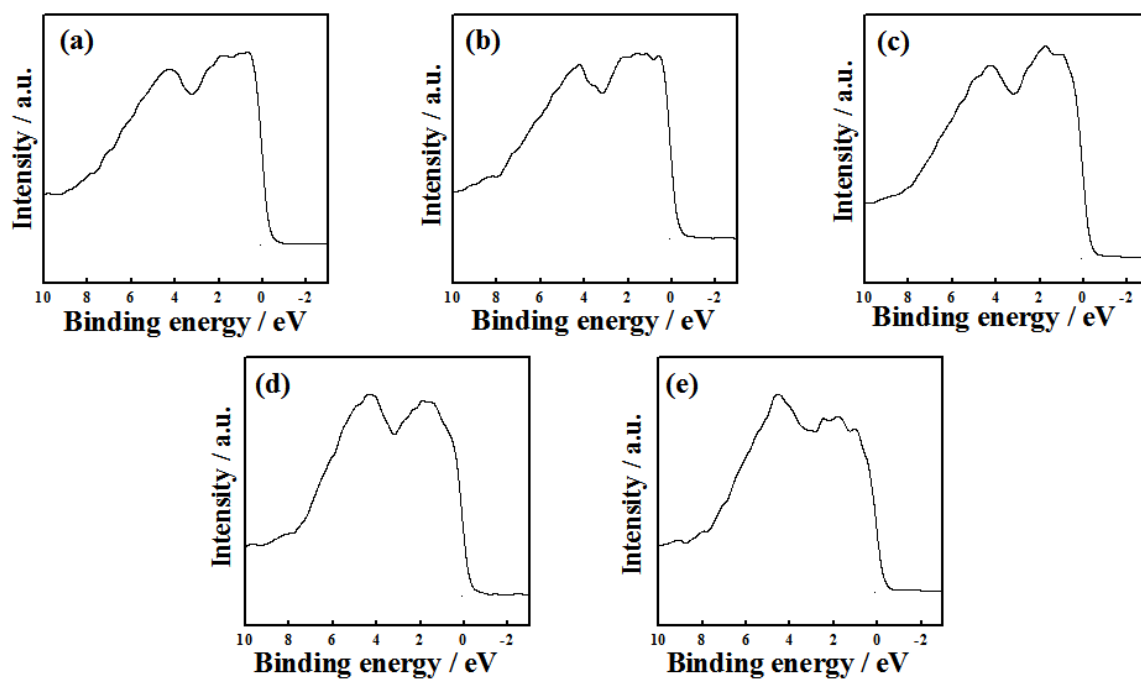
Figure S9. *The d-band center position obtained from the valence-band spectra of Pt₃M alloy electrodes*

relative to the Fermi level. (a) Pt, (b) Pt$_3$Zr alloy, (c) Pt$_3$La alloy, (d) Pt$_3$Fe alloy, and (e) Pt$_3$Ti alloy.
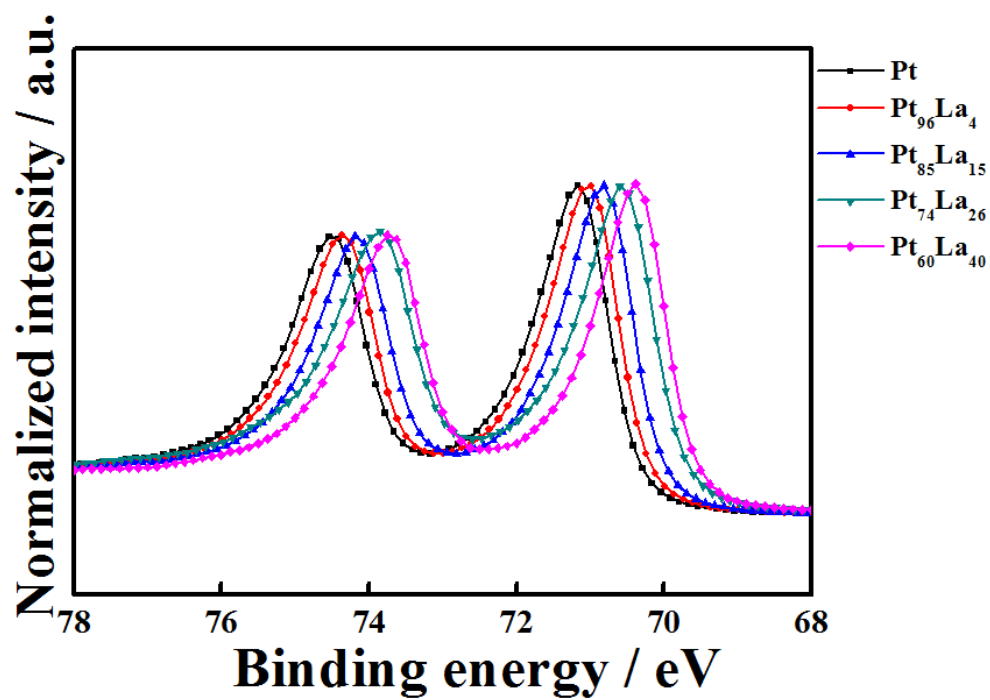
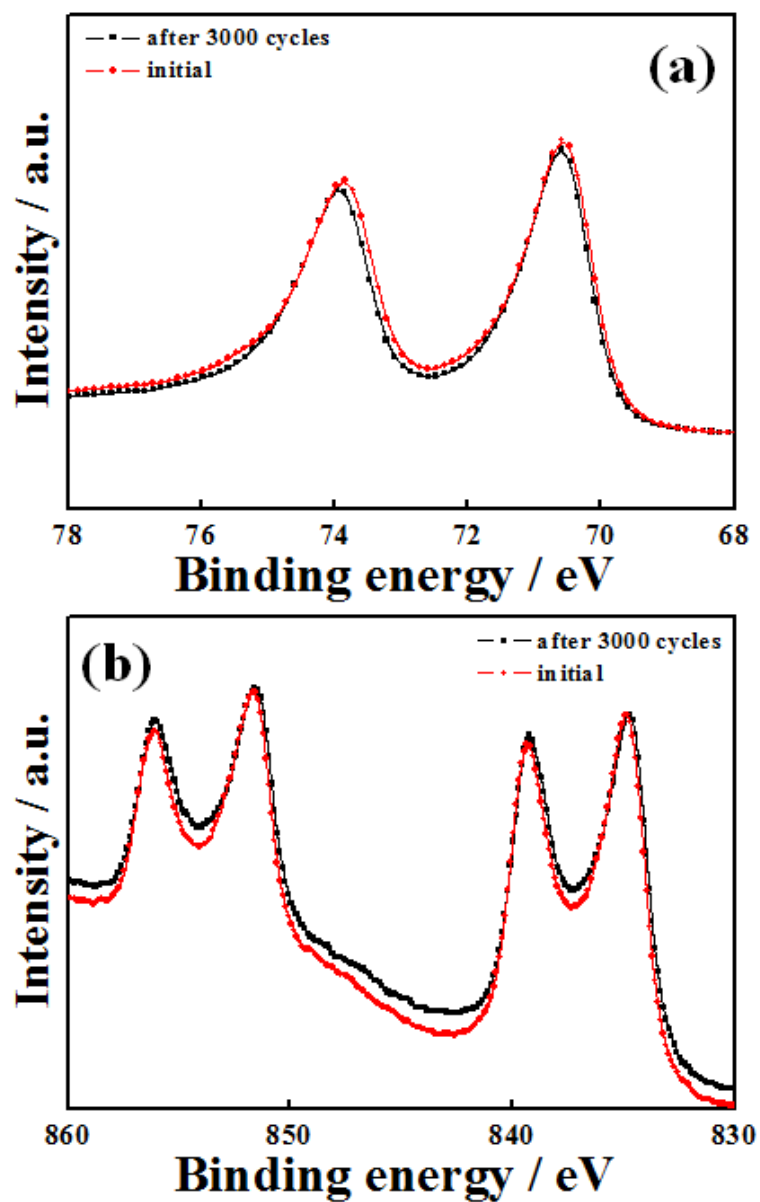**Figure S10**. *XPS spectra of PtLa allys electrodes*

Figure S11. *XPS spectra of Pt₃La alloy catalysts before and after potential cycles.(a) Pt 4f peaks and (b) La 3d peaks.*

6. Synchrotron X-ray absorption spectroscopy

To evaluate this argument, we measured X-ray absorption near-edge spectroscopy (XANES) on Pt_3M alloys, and we measured the Pt L_{III} edges. One significant aspect of the XANES analysis is that it can provide important information on the Pt d-band vacancy. The d-band vacancy is derived from the analysis of the Pt L_{III} and L_{II} white lines. The L_{II} and L_{III} edges are due to the excitation of the $2p_{1/2}$ and $2p_{3/2}$ electrons, respectively. These electrons can undergo transitions to empty states in the vicinity of the Fermi level. Since the dipole selection rules in the XANES region restrict the transitions to L = 1 and J = 0, 1 (where L and J are the orbital angular quantum number and the total angular quantum number, respectively), the transitions to the d-orbitals are strongly favored [3]. In the case of Pt, it has been shown that the contribution of the final states with J = 5/2 is 14 times more than the contribution with J = 3/2. The L_{III} transition ($2p_{3/2}$ to $5d_{5/2}$) is thus more highly favored by the selection rules than the L_{II} transition ($2p_{3/2}$ to $5d_{5/2}$) [4]. The intensity of the L_{III} peaks, and to a lesser extent the L_{II} peaks, increases with increasing Pt d-band vacancy [5]. X-ray absorption near edge structure (XANES) experiments were conducted on 7C1 beamline of Pohang Accelerator Laboratory (PAL) (2.5 GeV; 150-180 mA). The incident beam was monochromatized using a Si(111) double crystal monochromator and detuned by 30% to minimize the contamination from higher harmonics, in particular, the third order reflection of the silicon crystals. The spectra for L_{III}-edge of Pt (E_0 =11564 eV) were taken in a transmission mode with separate He-filled IC Spec ionization chambers for incident and transmitted beams, respectively. Before measuring samples, energy was calibrated by using of Pt foil. The energy scan was performed in five regions for good energy resolution in a steep absorption and measurement of XANES spectra at a time, 5 eV-step in region of 11364-11514 eV, 1 eV-step in 11514-11554 eV, 0.25 eV-step in 11554-11594 eV, 0.03 k-step in 11594-12104 eV, and 0.04 k-step in 12104-12564 eV. Pre-edge absorption due to the background and detector were subtracted using a linear fit to the data in the range of -200 to -60 eV relative to E_0. E_0 was defined as the first inflection point on the rising absorption edge. Each spectrum was then normalized by a constant, extrapolated value to E_0 of third-order polynomial fit over absorption

at 150-900 eV relative to E_0. The data analysis package used for XANES was the University of Washington's data analysis program. The XANES spectra were first subjected to background removal by fitting the pre-edge data to a Victoreen type formula over the range of -200 to 80 eV below the edge, followed by extrapolation over the energy range of interest and subtraction from the data. After the removal of the background contributions, the spectra were corrected for edge-shifts using the second derivatives of the inflection points of the data from the reference channel. The procedures used for normalization were the conventional ones. The normalization value was chosen as the absorbance at the inflection point of one EXAFS oscillation.
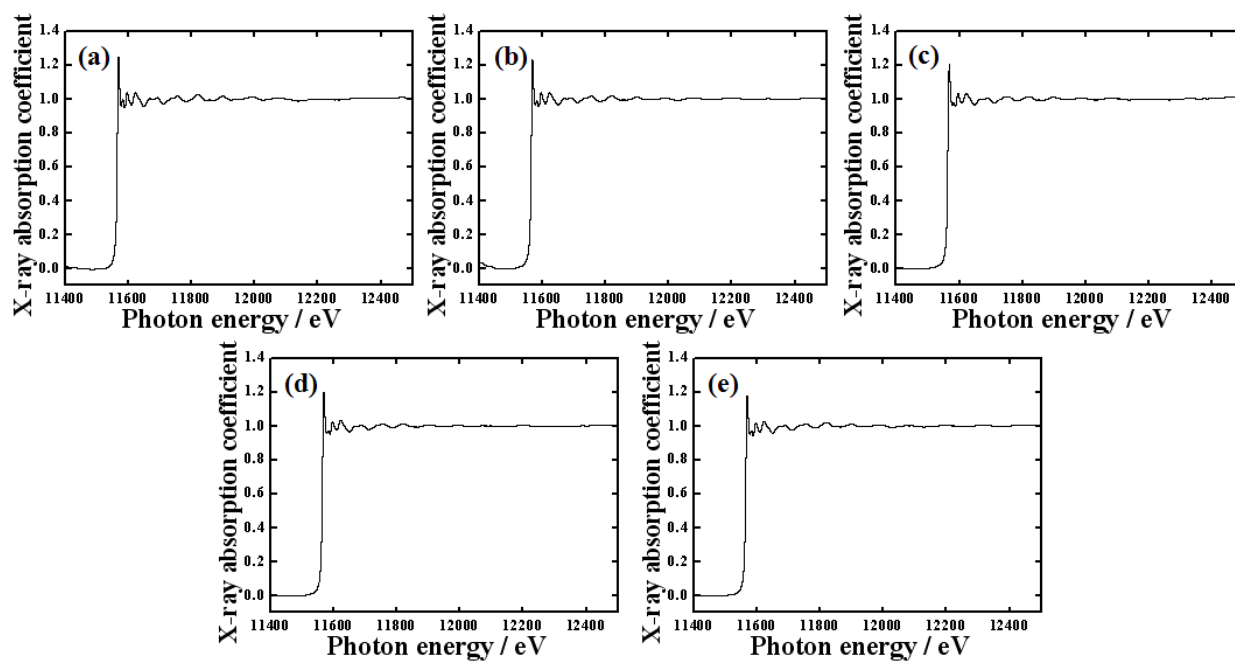
Figure S12. *XANES spectra of Pt-La alloy catalysts. (a) Pt foil, (b) $Pt_{96}La_4$, (c) $Pt_{85}La_{15}$, (d) $Pt_{74}La_{26}$,*

and (e) $Pt_{67}La_{33}$.

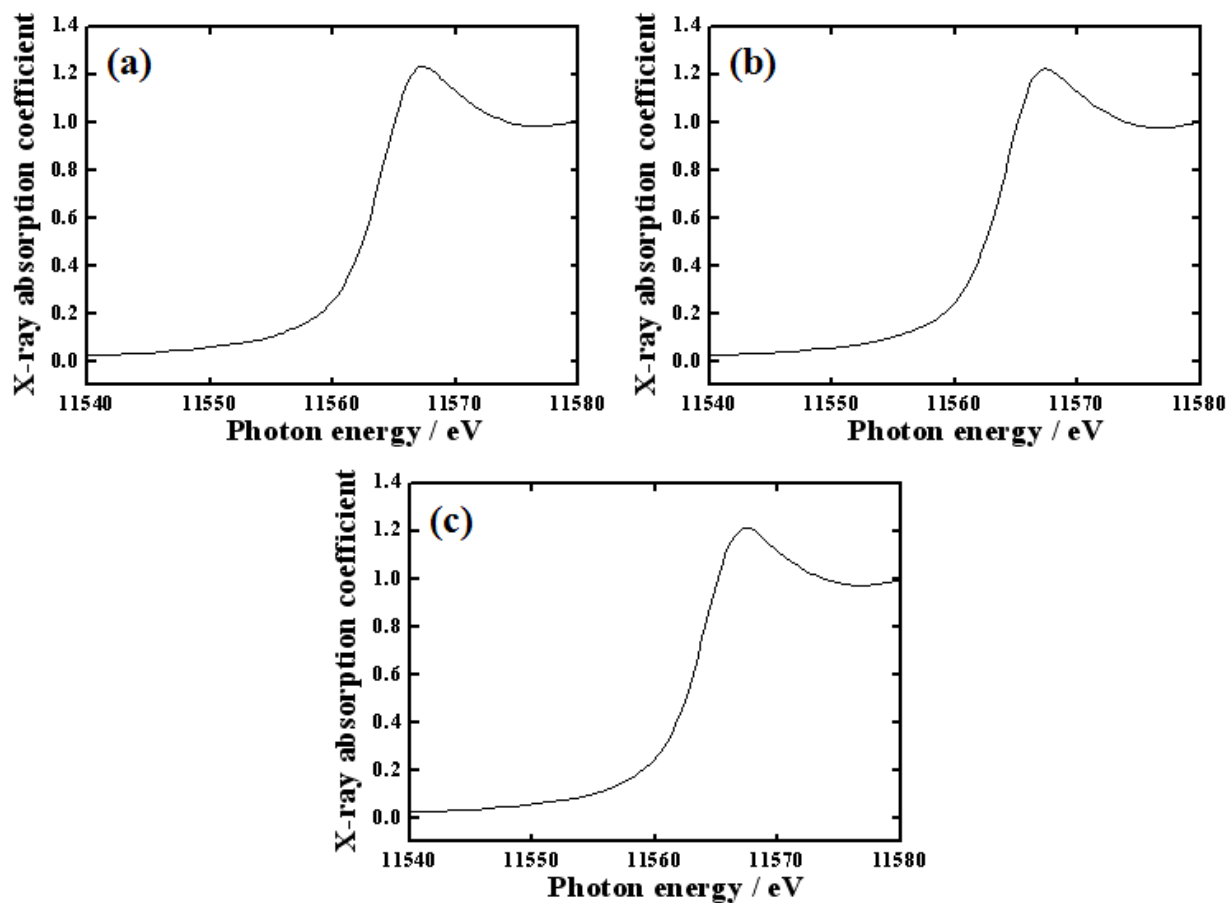***Figure S13.*** *XANES spectra of Pt₃M alloy catalysts. (a) Pt₃Fe, (b) Pt₃Zr, and (c) Pt₃Ti.*

7. Computation method using DFT calculation

7.1. Computational details

For both Pt(111) and Pt$_3$La(111) systems, all the calculations were carried out based on DFT, using the Vienna Ab-initio Simulation Package (VASP) [6,7]. A hexagonal 4×4 slab with five layers were generated as the substrate and a vacuum layer of 15 Å was added on the slab to simulate the surfaces within the periodic boundary condition. The top three layers were allowed to fully relax while the atoms in the fourth layer were only vertically relaxed. All the adatoms were set free so they can fully relax. The atoms in the bottom layer were fixed at their bulk lattice parameters (correspond to a = 3.977 Å for Pt and a = 4.240 Å for Pt$_3$La). All the adatoms were set free so they can fully relax.

The relaxations of the electrons were described by projector augmented wave (PAW) potentials [8,9] with the exchange-correlation energy of the Perdew–Burke–Ernzerhof (PBE) parameterization [10,11] within the generalized gradient approximation (GGA). An energy cutoff of 400 eV and the gamma-centered Monkhorst-Pack scheme [12] were used to generate a 4×4×1 k-point mesh until the total energy difference of the system between the consecutive iterating steps became less than 10^{-4} eV. The geometric structure was optimized by the quasi-Newton or conjugate gradient techniques until the Hellmann-Feynman forces were below 0.02 eVÅ^{-1}. Spin polarization and dipole correction were not considered in this study except the cases for individual atoms, because several selected runs showed that they do not contribute any significant difference in the calculation results.

The adsorption energies of each adatom, E_{ad}^{adatom}, were calculated using the following equation:

$$E_{ad}^{adatom} = -[E_{slab}^{adatom} - (E_{slab} + E_{atom})] \text{ --------------------------------------}(3)$$

where, E_{slab}^{adatom}, E_{slab}, and E_{atom} are the energy of slab with an adatom, that of the slab, and that of an isolated adatom, respectively. The positive adsorption energy indicates that the adsorption will occur

spontaneously, while the negative adsorption energy indicates that the adsorption process is not energetically favorable.

The formation energy of the mono-vacancy, E_v was calculated using the following equation:

$$E_v = (E^{slab}_{system-v} + E^{bulk}_{atom}) - E^{slab}_{system} \quad \text{----------------------------} \quad (4)$$

where, $E^{slab}_{system-v}$, E^{bulk}_{atom}, and E^{slab}_{system} are the energy of the slab system with one vacancy, that of the constituting atom in bulk, and that of the slab system, respectively.

7.2. Results

7.2.1. Computational results of La

7.2.1.1. La-atom

E_0 = -0.7507 eV mag = 1.0000

7.2.1.2. La-hcp

La: P63/mmc (Space group number: 194), HCP

a_0 = 3.68: -19.4939/4 = -4.8734 at z-vector = 3.212

a_0 = 3.73: -19.5554/4 = -4.8888 at z-vector = 3.212

a_0 = 3.78: -19.5787/4 = -4.8946 at z-vector = 3.212

a_0 = 3.83: -19.5632/4 = -4.8908 at z-vector = 3.212

a_0 = 3.88: -19.5132/4 = -4.8783 at z-vector = 3.212

z-vector = 3.20, a_0 = 3.78: -19.5778

z-vector = 3.22, a_0 = 3.78: -19.5785/4 = -4.894625 → c/a = 1.61

z-vector = 3.23, a_0 = 3.78: -19.5783

z-vector = 3.24, a_0 = 3.78: -19.5777

7.2.1.3. Properties at a_0 = 3.78, c/a = 1.61

E_{coh} = -4.894625 –(-0.7507) = -4.14 eV (= 4.14 eV)

E_{coh} = 4.23 eV by other DFT/PBE, exp = 4.467 eV

B = 28 Gpa from webelements

7.2.2. Computational results of Pt_3La

7.2.2.1. FCC-lattice

$$d^2E/da^2 = d^2(33808.931\ a^2 - 5301.1607\ a^3 + 311.74052\ a^4)/da^2$$

$$= (2)(33808.931) + (3)(2)(-5301.1607)(4.24) + (4)(3)(311.74052)(4.24)(4.24)$$

$$= 67617.862 - 134861.528208 + 67252.156468224 = 8.49\ eV/Å^2$$

B = 4x8.49 /9(4.24) = 0.89 eV/ Å3 = 142.6 Gpa, 1 eV/ Å3 = 160.2176487 Gpa

E_0 = -26.500160 eV/4-atom lattice = -6.625 eV/atom at a = 4.240

E_{coh} = -26.500160 –(-0.5947x3) –(-0.7507) = -5.99 eV (= 5.99 eV)

7.2.2.2. FCC-lattice-accurate

a = 4.238: -26.500088

a = 4.240: -26.500167 = -6.625 eV/atom, -26.500167/mag = 0.0001 with spin

a = 4.242: -26.500098

H_f = **-26.50017** -(-6.058x3)-(-4.894625) = -3.43 eV/system = -0.86 eV/atom

7.2.2.3. Slab

a = 4.240 → a_0 = 2.998, c/a = 1.62

E_0 = -511.3442 eV/system

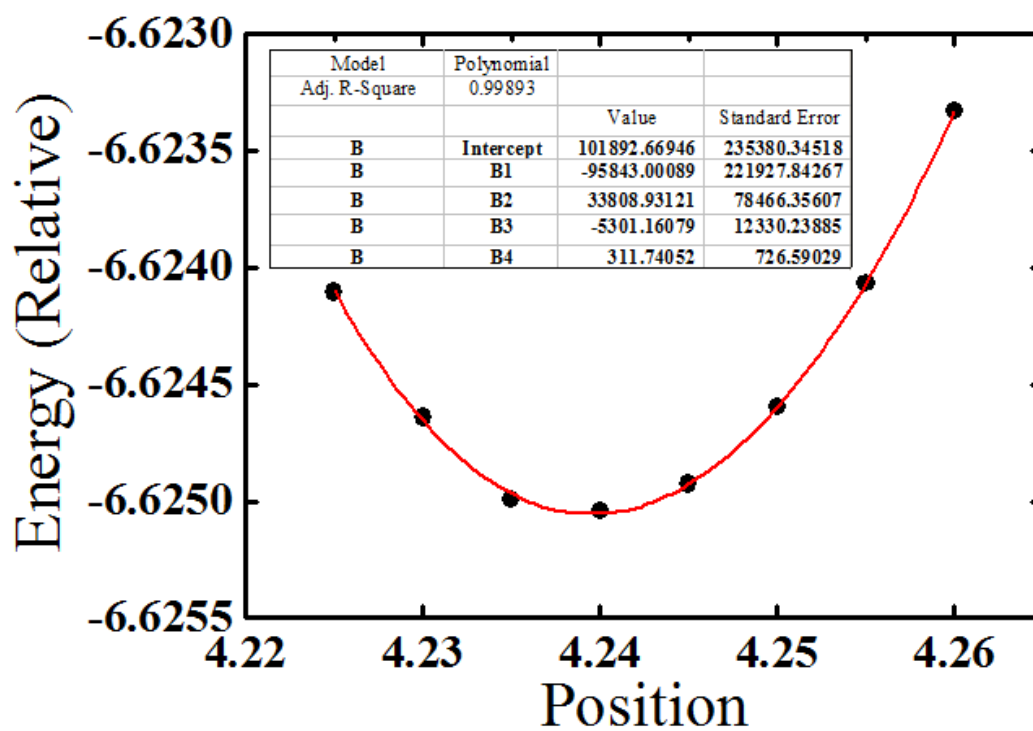| Model	Polynomial		
Adj. R-Square	0.99893		
		Value	Standard Error
B	Intercept	101892.66946	235380.34518
B	B1	-95843.00089	221927.84267
B	B2	33808.93121	78466.35607
B	B3	-5301.16079	12330.23885
B	B4	311.74052	726.59029

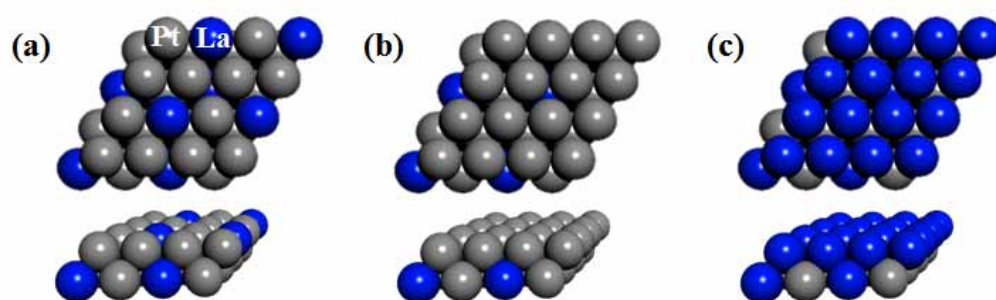**Figure S14.** *Equilibrium energy of Pt-La alloy as function of lattice parameter.*

Figure S15. *Schematic diagrams of (a) Pt₃La, (b) surface-all-Pt, and (c) surface-all-La on Pt₃La slab.*

Table S1. *Surface segregation of (a) Pt₃La, (b) surface-all-Pt, and (c) surface-all-La on Pt₃La slab.*

	(a) Pt$_3$La	(b) Surface-all-Pt on Pt$_3$La	(c) Surface-all-La on Pt$_3$La
ΔE_{se} (eV)	-	6.324	1.988

Table S2. *Cohesive energy of Pt and La on Pt₃La slab.*

	(a) Pure Pt	(b) Pure La	(c) Pt$_3$La
E_{coh} (eV / atom)	5.53	4.14	5.99

7.2.3. Vacancy formation on surface

7.2.3.1. Pt$_3$La-1vcancy-La slab with bulk fcc parameters

(a_0 = 2.998, c/a = 1.62)

E_v^f = -501.1723 +511.3442 -0.7507 = 9.4212 eV

7.2.3.2. Pt$_3$La-1vacancy-Pt slab with bulk fcc parameters

(a_0 = 2.998, c/a = 1.62)
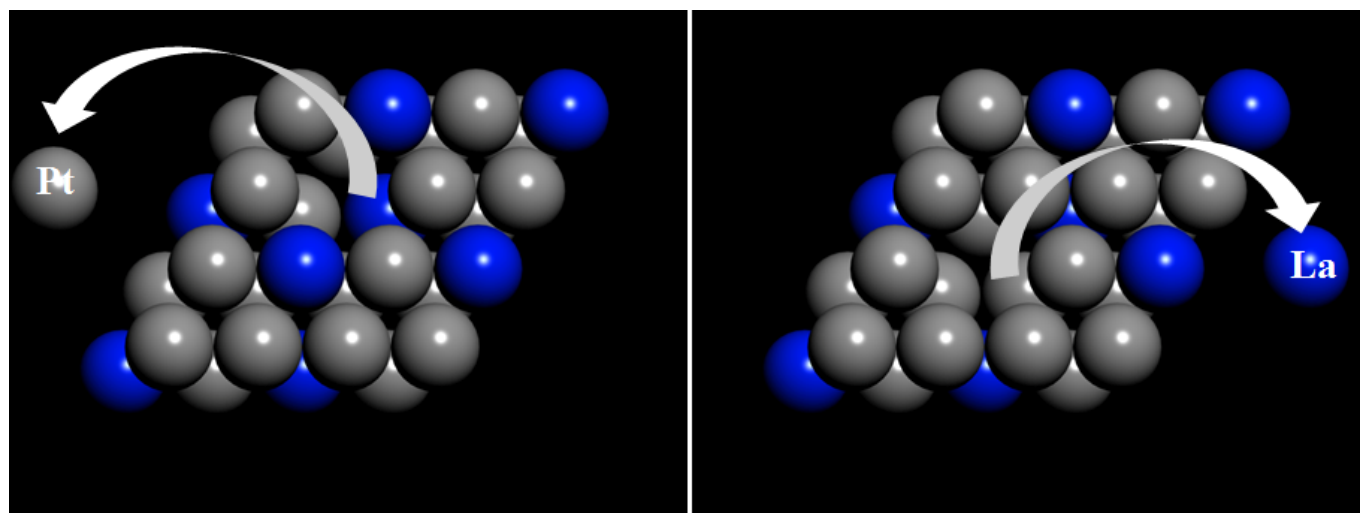
E_v^f = -505.1000 +511.3442 -0.5947 = 5.6495 eV

Figure S16. Schematic diagram of (a) Pt and (b) La dissociation on Pt₃La slab.

Table S3. *Dissociation energy of Pt and La on Pt₃La slab.*

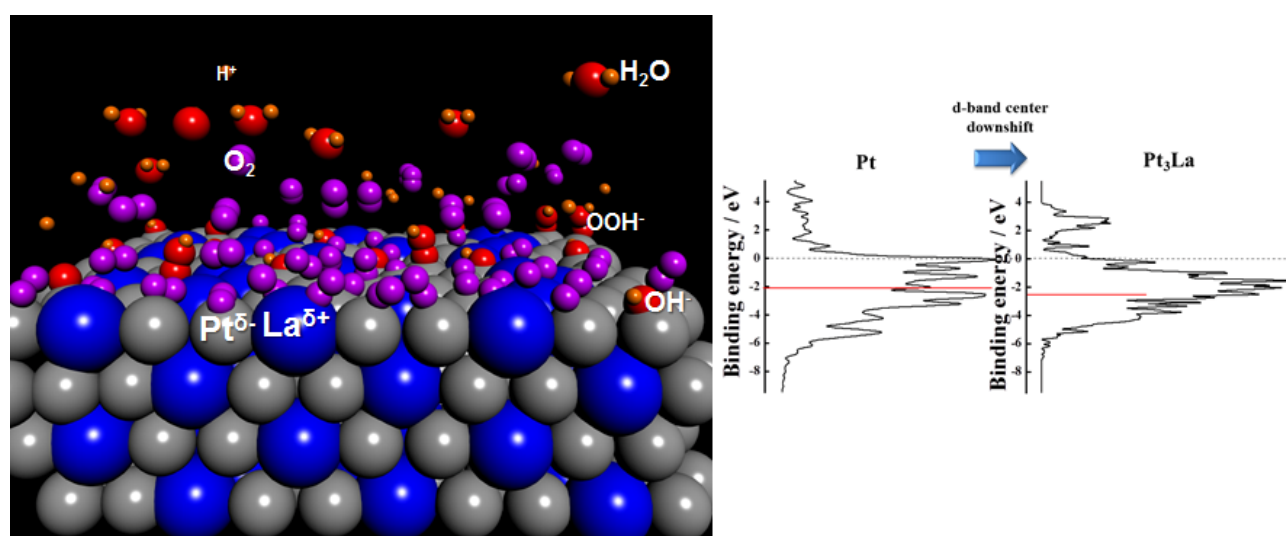|	Pt on Pt$_3$La	La on Pt$_3$La
E_d (eV /atom)	5.6495	9.421

Figure S17. *Schematic diagram of Pt₃La electrode and Projected DOS of Pt and Pt₃La.*

8. The stability of Pt₃La electrodes in acid electrolyte

Evidence for the stability of Pt$_3$La as employed in this paper is provided in Figure S18, which is a depth profile of the Pt$_3$La sample, constructed from angle resolved x-ray photoelectron spectroscopy data. This was taken after soaking the sample in an electrochemical cell (0.1 M HClO$_4$ electrolyte) for 2 hrs. Figure S18(a) and (b) show the intensity of the Pt 4f and La 3d peaks, as a function of the angle of the analyzer to the surface normal. In the process of transferring the catalyst surface from the electrochemical cell to the XPS analysis chamber, the surface would have been contaminated with an adventitious layer of organic matter, arising from the laboratory atmosphere. This is unlikely to be present under reaction conditions. Consequently, both the Pt and La peaks are very low in intensity at high angles, where the analysis mainly probes the immediate vicinity of the surface. However, both the Pt and the La peaks increase in intensity with decreasing angle, as the measurement probes deeper below the surface. The depth profile in Figure S18(c) is constructed by a model which combines the data shown in Figure S18(a) and Figure S18(b), along with the corresponding peaks for C and O. Notably, at the surface, there is a very small Pt and La signal, and a large C and O signal, supporting notion that there is an over-layer composed of organic contamination. However, the Pt peak and La peak hold up to the ratio of 75 % and 25 % relative intensity, respectively, where the C and O signal is negligible. This provides clear evidence that there is a homogeneous composition at the catalyst surface and bulk in acid electrolyte.
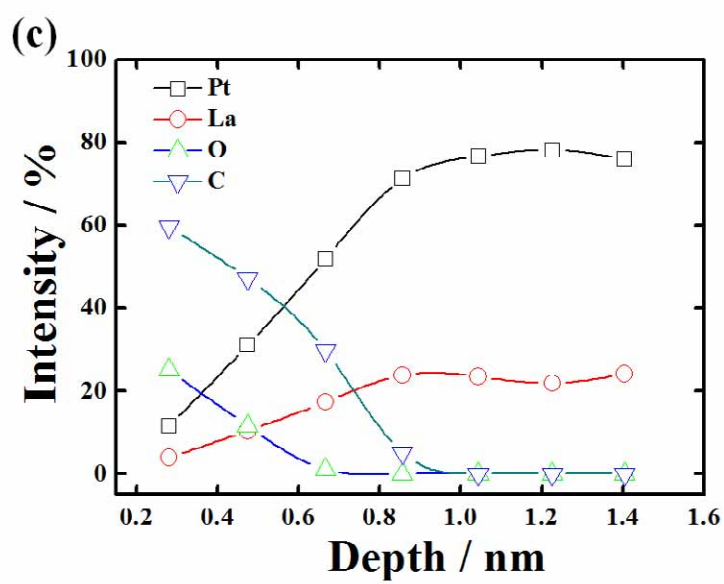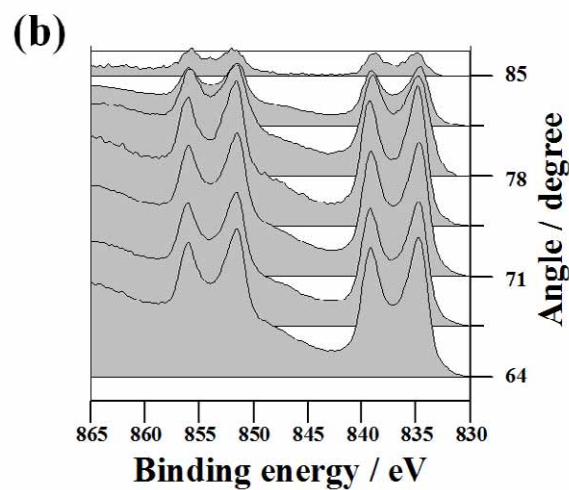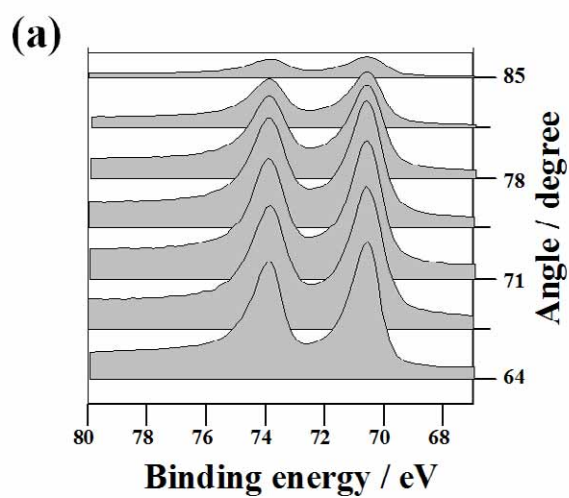
Figure S18. *Angle resolved XPS data for (a) Pt 4f and (b) La 3d on Pt₃La electrode and (c) depth*

profiles.

References

[1] W. P. Zhou, A. Lewera, R. Larsen, R. I. Masel, P. S. Bagus, A. Wieckowski, *J. Phys. Chem. B* **2006**, *110*, 13393.

[2] V. R. Stamenkovic, B. Fowler, B. S. Mun, G. F. Wang, P. N. Ross, C. A. Lucas, N. M. Markovic, *Science* **2007**, *315*, 493.

[3] L. M. Falicov, W. Hanke, M. P. Maple, *Valence Fluctuation in Solids*, Nprth-Holland Pub., Amsterdam, **1981**.

[4] A. E. Russell, S. Maniguet, R. J. Mathew, J. Yao, M. A. Roberts, D. Thompsett, *J. Power Sources* **2001**, *96*, 226.

[5] A. N. Mansour, J. W. Cook, D. E. Sayers, *J. Phys. Chem.* **1984**, *88*, 2330.

[6] G. Kresse and D. Joubert, *Phys. Rev. B*. **1999**, *59*, 1758.

[7] http://cms.mpi.univie.ac.at/vasp, **2010**.

[8] G. Kresse and J. Furthmüller, *Comp. Mater. Sci.* **1996**, *6*, 15.

[9] P. E. Blöchl, *Phys. Rev. B*. **1994**, 5*0*, 17953.

[10] J. P. Perdew, K. Burke, and M. Ernzerhof, *Phys. Rev. Lett.* **1996**, *77*, 3865.

[11] B. Hammer, L. B. Hansen and J. K. Nørskov, *Phys. Rev. B*. **1999**, *59*, 7413.

[12] H. J. Monkhorst and J. D. Pack, *Phys. Rev. B*. **1976**, *13*, 5188.